

Deep geophysical anomalies beneath the Changbaishan Volcano

Shaohua Li¹, Jiaqi Li², Thomas P. Ferrand³, tong zhou⁴, Mingda Lv⁵, Ziyi Xi⁵, Ross Maguire⁶, Guangjie Han⁷, Juan Li⁸, Xiyuan Bao², Yiran Jiang⁹, and tiezhao bao¹⁰

¹Lanzhou Institute of SeismologyCEA

²University of California, Los Angeles

³Freie Universität Berlin

⁴Aramco Research Center Beijing

⁵Michigan State University

⁶University of Maryland

⁷China Earthquake Networks Center

⁸Institute of Geology and Geophysics, Chinese Academy of Sciences

⁹Peking University

¹⁰CNOOC Research Institute

November 23, 2022

Abstract

Subsurface imaging is key to understanding the origin of intraplate volcanos. The Changbaishan volcano, located about 2000 km away from the western Pacific subduction zone, has several debated origins. To investigate this, we compared regional seismic tomography with the electrical resistivity results and performed high-resolution 1D and quasi-2D velocity-depth profiles. We show that the upper mantle is characterized by two anomalies exhibiting distinct features which cannot be explained by the same mechanism. We document a localized low-velocity anomaly atop the 410-km discontinuity, where the P-wave velocity is reduced more than that of the S-wave (i.e., low V_p/V_s). We propose that this anomaly is caused by the reduction of the effective moduli during the phase transformation of olivine. The other anomaly, located between 300 km and 370 km depth, reveals a significant reduction of the S-wave velocity (i.e., high V_p/V_s), associated with a reduction of the electrical resistivity, altogether consistent with partial melting.

Supplementary Material for

Deep geophysical anomalies beneath the Changbaishan Volcano Shaohua Li^{1, 2}, Jiaqi Li^{3, *}, Thomas P. Ferrand⁴, Tong Zhou⁵, Mingda Lv⁶, Ziyi Xi⁷, Ross Maguire⁸, Guangjie Han^{9, 10, 11}, Juan Li^{10, 11, 12}, Xiyuan Bao³, Yiran Jiang¹³, and Tiezhao Bao¹⁴

1 Gansu Lanzhou Geophysics National Observation and Research Station, Lanzhou, 730000, China

2 Lanzhou Institute of Seismology, China Earthquake Administration, Lanzhou, 730000, China

3 Department of Earth, Planetary, and Space Sciences, University of California, Los Angeles, CA 90095, USA. E-mail: jli@epss.ucla.edu

4 Institut für Geologische Wissenschaften, Freie Universität Berlin, Malteserstraße 74-100, Berlin, Germany.

5 Aramco Research Center – Beijing, Aramco Asia

6 HPCAT, X-ray Science Division, Argonne National Laboratory, Argonne, IL 60439

7 Department of Computational Mathematics, Science and Engineering, Michigan State University, East Lansing, MI 48824, USA

8 University of Illinois at Urbana-Champaign, Champaign, IL, USA

9 China Earthquake Networks Center, Beijing, China

10 Key Laboratory of Earth and Planetary Physics, Institute of Geology and Geophysics, Chinese Academy of Sciences, Beijing, China

11 College of Earth and Planetary Sciences, University of Chinese Academy of Sciences, Beijing, China

12 Heilongjiang Mohe Observatory of Geophysics, Institute of Geology and Geophysics, Chinese Academy of Science, Beijing, China

13 School of Earth and Space Sciences, Peking University, Beijing 100871, China;

14 CNOOC Research Institute, Beijing, China

Summary

There are one figures in this supplementary material.

We discussed the mismatches and the influences at smaller epicentral distances between the synthetics and the data for the S waves. To conclude, we interpreted it as caused by the possible noise in the data. This is because of the second peak in the waveform for stations LN.GAX or LN.BZH is of a higher frequency (i.e., shorter during), which is inconsistent with other stations. In addition, this second peak suddenly disappears for stations at slightly smaller distances. We also performed another inversion without stations LN.GAX and LN.BZH. Results show (Fig. S1) that the waveform fitting at a smaller distance is better, and the inverted models are almost unchanged.

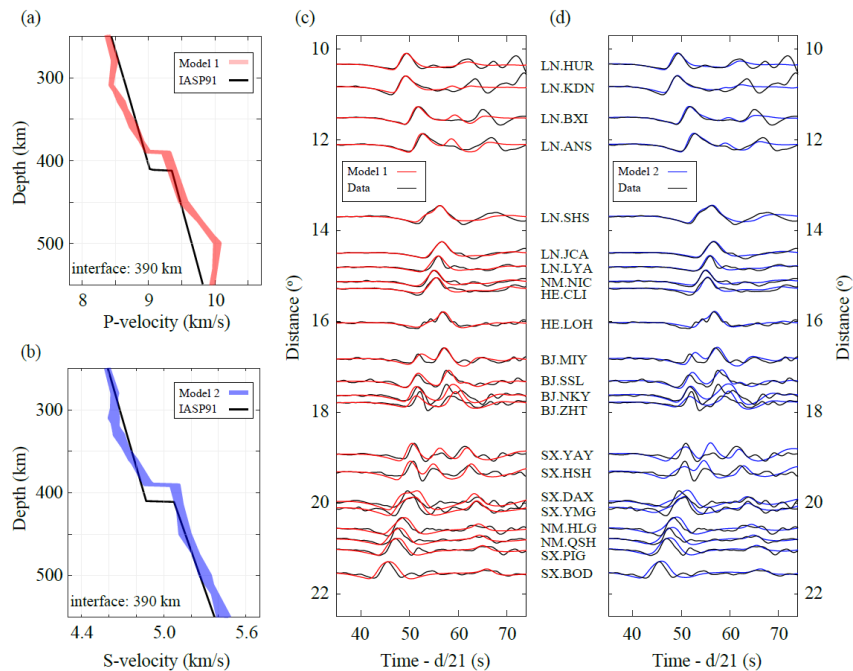


Figure S1

1. S-wave model comparisons between the ISAP91 model (in black) and the other model sets (i.e., model 1) whose synthetics show a mismatch (i.e., a second phase) for stations LN.BXI and LN.ANS.
2. S-wave model comparisons between the ISAP91 model (in black) and the other model sets (i.e., model 2) whose synthetics match the waveforms well for stations LN.BXI and LN.ANS.
3. Waveform comparisons between the data (in black) and the synthetics corresponding to model 1 in Fig. S1a (in red).
4. Waveform comparisons between the data (in black) and the synthetics corresponding to model 2 in Fig. S1b (in blue).

Hosted file

essoar.10512466.1.docx available at <https://authorea.com/users/543779/articles/601399-deep-geophysical-anomalies-beneath-the-changbaishan-volcano>

Deep geophysical anomalies beneath the Changbaishan Volcano

Shaohua Li^{1, 2}, Jiaqi Li^{3, *}, Thomas P. Ferrand⁴, Tong Zhou⁵, Mingda Lv⁶, Ziyi Xi⁷, Ross Maguire⁸, Guangjie Han^{9, 10, 11}, Juan Li^{10, 11, 12}, Xiyuan Bao³, Yiran Jiang¹³, and Tiezhao Bao¹⁴

1 Gansu Lanzhou Geophysics National Observation and Research Station, Lanzhou, 730000, China

2 Lanzhou Institute of Seismology, China Earthquake Administration, Lanzhou, 730000, China

3 Department of Earth, Planetary, and Space Sciences, University of California, Los Angeles, CA 90095, USA. E-mail: jli@epss.ucla.edu

4 Institut für Geologische Wissenschaften, Freie Universität Berlin, Malteserstraße 74-100, Berlin, Germany.

5 Aramco Research Center -- Beijing, Aramco Asia

6 HPCAT, X-ray Science Division, Argonne National Laboratory, Argonne, IL 60439

7 Department of Computational Mathematics, Science and Engineering, Michigan State University, East Lansing, MI 48824, USA

8 University of Illinois at Urbana-Champaign, Champaign, IL, USA

9 China Earthquake Networks Center, Beijing, China

10 Key Laboratory of Earth and Planetary Physics, Institute of Geology and Geophysics, Chinese Academy of Sciences, Beijing, China

11 College of Earth and Planetary Sciences, University of Chinese Academy of Sciences, Beijing, China

12 Heilongjiang Mohe Observatory of Geophysics, Institute of Geology and Geophysics, Chinese Academy of Science, Beijing, China

13 School of Earth and Space Sciences, Peking University, Beijing 100871, China;

14 CNOOC Research Institute, Beijing, China

Abstract

Subsurface imaging is key to understanding the origin of intraplate volcanos. The Changbaishan volcano, located about 2000 km away from the western Pacific subduction zone, has several debated origins. To investigate this, we compared regional seismic tomography with the electrical resistivity results and performed high-resolution 1D and quasi-2D velocity-depth profiles. We show that the upper mantle is characterized by two anomalies exhibiting distinct features which cannot be explained by the same mechanism. We document a localized low-velocity anomaly atop the 410-km discontinuity, where the P-wave velocity is reduced more than that of the S-wave (i.e., low V_p/V_s). We propose

that this anomaly is caused by the reduction of the effective moduli during the phase transformation of olivine. The other anomaly, located between 300 km and 370 km depth, reveals a significant reduction of the S-wave velocity (i.e., high V_p/V_s), associated with a reduction of the electrical resistivity, altogether consistent with partial melting.

Keywords intraplate volcano, low-velocity anomaly, partial melting, effective moduli

Plain Language Summaries

The Changbaishan volcano, located about 2000 km away from the western Pacific subduction zone, has several debated origins of volcanism. To investigate this, we compared regional seismic tomography with the electrical resistivity results and performed high-resolution 1D and quasi-2D velocity-depth profiles. We show that the upper mantle is characterized by two seismic velocity anomalies exhibiting distinct features which cannot be explained by the same mechanism. The anomaly located between 300 km and 370 km depth (with a high V_p/V_s ratio, but a reduction of the electrical resistivity) is associated with partial melting. This partial melting can originate either from deep hydration due to the dehydration of the Pacific slab in the mantle transition zone, or the buoyant materials coming from the possible gap of the slab. However, the other localized low-velocity anomaly atop the 410-km discontinuity (with a low V_p/V_s ratio) cannot be explained by partial melting alone and is likely caused by the reduction of the effective moduli during the phase transformation between olivine and wadsleyite.

Key Points:

- The upper mantle beneath the Changbaishan volcano is characterized by two seismic low-velocity anomalies.
- The shallow low-velocity anomaly (i.e., shallow than 370 km, with a high V_p/V_s ratio) is due to partial melting.
- The deep anomaly (i.e., atop the 410-km, with a low V_p/V_s ratio) is likely caused by the moduli reduction during the phase transformation.

1. Introduction

The Changbaishan volcano is the largest intraplate volcanic region in northeast China, and it is located more than 2000 km from the trench of the western Pacific subduction zone (Fig. 1a). Due to its large distance from the convergent boundary, the origin of the magmatism cannot be simply explained by plate tectonics (Tang et al., 2014). One early study by Tatsumi et al. (1990) proposed that an injection of the asthenosphere upwelling, associated with the opening of the Japan Sea, would explain the formation of the Changbaishan volcano. With

the development of seismic tomography, i.e., a technique to provide 2-D or 3-D seismic images of the deep Earth, structures down to the mantle transition zone provide new clues for the origin of intraplate volcanism.

Using P-wave travel times, Huang & Zhao (2006) and Chen & Pei (2010) observed a flat Pacific slab in the mantle transition zone that extended eastwards up to 2000 km from the trench. Zhao et al. (2009) and Kuritani et al. (2011) proposed that the origin of the Changbaishan volcano is related to the dehydration of the flat (stagnant) slab in the mantle transition zone. However, the expected island-arc signatures in the erupted rocks are absent indicated by geochemical studies (e.g., Chen et al. 2007; Zou et al. 2008). Using differential travel time between the P-waves (or S-waves), Tang et al (2014) identified a gap in the flat slab and proposed that mantle upwellings (i.e., low-velocity anomalies in seismic tomography images, possibly originated from below the 660-km discontinuity) and the subsequent decompression melting at asthenosphere depths could feed the Changbaishan volcano through the gap in the slab. Although the methods employed were effective at providing the first seismic velocity models for the area, the resolution from travel-time tomography is too sparse to resolve deep structures in detail.

With increasing computation power, the development of efficient 3-D waveform simulation tools (Komatitsch & Tromp, 1999), and advances in inversion theory (Tromp et al., 2005), seismic tomography studies utilizing the full-waveform information have become feasible in both regional and global scales (e.g., Bozdogan et al., 2016; Chen et al., 2015; Fichtner et al., 2009; French & Romanowicz, 2014; Tape et al., 2009; Zhu et al., 2015; Lei et al., 2020). The regional tomographic model FWEA18 (Tao et al. 2018) has the currently highest resolution, among the full-waveform inversion models, in East Asia, derived from a dataset consisting of both body waves and surface waves.

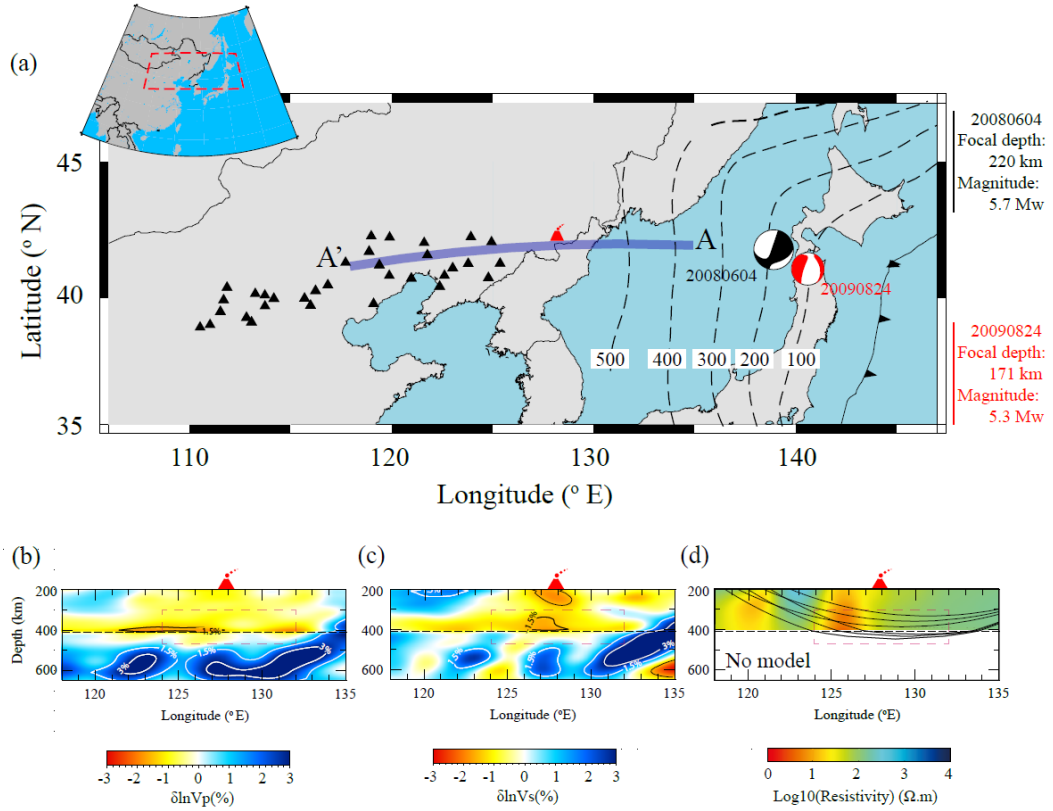
The high-resolution images from the FWEA18 model make it possible to further study the detailed subsurface structures down to the mantle transition zone. More importantly, it also provides an opportunity to combine the P- and S-wave models to decipher the origin of the Changbaishan volcano. For example, either the presence of volatiles (e.g., water) or high temperature could reduce the P- and S-wave speeds, but in different ways (Tseng & Chen, 2008). Specifically, from the laboratory measurement of the polymorphs of olivine, the effect of the temperature on the P- and S-wave speeds are comparable (Kern, 1982; Sino-geikin et al., 1998; Jackson et al., 2000). On the contrary, hydration of crystal lattices or grain boundaries will cause twice a reduction in the S-wave speed than the P-wave speed (Faul et al., 1994; Toomey et al., 1998).

In the cross-section along the down-dip direction and cutting through the Changbaishan volcano, the FWEA18 model shows distinct features in the P- and S-wave models. In the P-wave model (Fig. 1b) the low-velocity anomaly is mainly concentrated in the vicinity of the top of the 410-km discontinuity with a maximum amplitude of -1.5%, whereas at depths between 300 km and 370 km there are very few low-velocity anomalies (i.e., less than -1%). In the S-wave model,

there is also a low-velocity anomaly atop the 410-km of similar or even smaller amplitude (i.e., about -1.0 to -1.5%) as that in the P-wave model. However, at shallower depths (i.e., 300 km – 370 km), there are strong low-velocity anomalies (i.e., -1.5%) in the S-wave models and those anomalies are distributed over a large depth range.

If such distinct behaviors in the P- and S-wave models are true features, this will indicate the low-velocity anomaly atop the 410-km and the other one at a shallower depth (i.e., 300 km – 370 km) likely operate by different mechanisms. However, although the FWEA18 model is currently the full-waveform inversion model with the highest resolution in this region, its resolution is still limited due to the lack of short-period seismic data which is prohibited by the large computational costs of 3D simulations. For example, the shortest period is 8 s for the P-wave, and the corresponding resolution is about 50 – 80 km (Tao et al., 2017).

To figure out whether the features in the FWEA18 model are valid or correspond to artifacts due to resolution issues, we have to analyze seismic data at a higher frequency (i.e., better spatial resolution). Therefore, we aim to perform 1D and quasi-2D waveform inversions with high-frequency data (i.e., the shortest period down to 2 s) to provide a more accurate 1D velocity-depth profile as an ‘anchor point’ in the cross-section of the tomographic FWEA18 model (i.e., the average 1-D model in the dashed box in Fig. 1b and c).



2. Data and Method

2.1 Data

We selected two high-quality datasets corresponding to two particular earthquakes recorded by a sub-linear seismic array in the same cross-section (Fig. 1a). These two earthquakes occurred at a similar location beneath the Japan Sea, but with different focal depths (Ekström et al., 2012). The first event 20080604 occurred on June 4th, 2008 with a moment magnitude of 5.7 and a focal depth of 220 km (Han et al., 2021). This relatively large event produced both clear P- and S-wave triplications recorded by dense seismic stations in China (Fig. 1a). The second event 20090824 occurred on August 24th, 2009 with a moment magnitude of 5.3 and a focal depth of 171 km. For this event with a relatively smaller magnitude, only clear P-wave signals are recorded.

We download the continuous waveform data (300s and 1200 s before and after the theoretical P-wave arrival) and use the Seismic Analysis Code (SAC) to remove the instrument response, with a pre-filtering from 0.01 to 8 Hz to get the displacement records (Fig. 2). We prefer to use the displacement data in

this triplication work. Finally, we band-pass filtered (from 0.04 to 1 Hz for the P-wave data, and 0.05 to 1 Hz for the S-wave data) the displacement data with a zero-phase, 2nd-order Butterworth filter.

2.2 Methods

2.2.1 Body wave triplications

Body wave triplication is sensitive to the structures near the discontinuity due to the dense ray paths (e.g., Stähler et al., 2012; Takeuchi et al., 2014; Bissig et al., 2022). It also has the advantage of isolating the anomaly near the turning points from the entire ray paths, since different triplicated phases share almost the same paths near the source and receiver but are separated at the turning points (penetration depths). Therefore, triplication is an effective tool to sample the low-velocity anomaly at the target region (i.e., from 300 km to 450 km).

However, there are also tradeoffs between model parameters, i.e., different models yield very similar triplication waveforms (Shearer, 2000). The most important tradeoff, which will influence our measurement of the low-velocity anomalies is the one between the size of the low-velocity zone (i.e., the wave speed reduction of the low-velocity anomaly and its thickness) and the location of the 410-km discontinuity. For example, triplication observations are similar between a large reduction of wave speed with an uplifted 410-km discontinuity and a small low-velocity anomaly with a depressed interface, as demonstrated via synthetic data by Li et al. (2022).

To consider this important tradeoff, we varied the discontinuity depth from 380 to 440 km with an interval of 10 km. And at each discontinuity depth, we performed an individual inversion. The final results and discussions are based on the model ensembles from these inversions.

2.2.2 1D Inversion scheme

We invert both P-wave and S-wave triplication data using the FastTrip software (Li et al., 2021). FastTrip is an open-source triplication phase inversion package that is based on QSEIS (Wang 1999) and the Niching Genetic Algorithm (Koper et al., 1999) for the 1D forward modeling and model selection, respectively. In the forward modeling part, we stacked the first arrival of the P-wave at larger distances (i.e., 20-22 degrees) to represent the source time function for the P-waves. For the S-wave, we convolved the P-wave source time function with a constant t^* value of 3 s to simulate the effect of attenuation of the S-waves (Stein and Wysession, 2009). We note that the choice of the source time function and the attenuation factor (i.e., t^*) will not affect the inversion results much because we focused more on the differential travel time and amplitudes between the triplicated waveforms, rather than the individual pulses.

With FastTrip, we can achieve better waveform fittings for array data than the trial-and-error approach, reveal the tradeoffs between model parameters, and

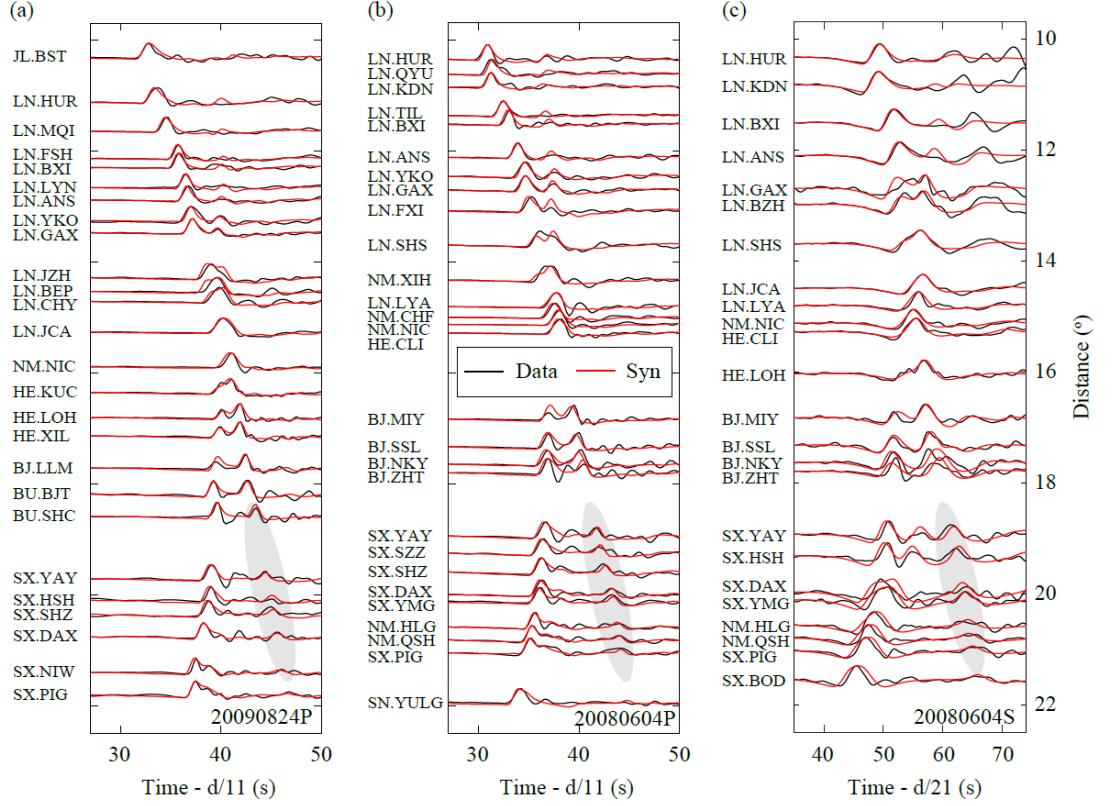
quantitatively analyze the uncertainty ranges. With 100 CPUs, one inversion cycle (10,000 waveform simulations and model selections) with 13 unknown model parameters can be completed within hours.

3. Results

3.1 Waveform fitting

Fig. 2a and b exhibit the waveform comparison between the recorded (black) and synthetic (red) waveforms, for the P-waves on the vertical component for events 20090824 and 20080604, respectively. Fig. 2c shows the SH-waves for event 20080604 on the tangential component. Synthetic waveforms for P- and SH- waves are calculated using independent P- and SH-wave speed models (the average value of the models in Fig. 3b and Fig. 3d, respectively). The synthetics correlate well with the data, with an average cross-coefficient higher than 0.9 and 0.8 for the P- and S-waves, respectively. Both the relative arrival time and amplitude between the triplicated phases are well-matched for most of the stations, indicating the reliability of the structures near the 410-km discontinuity.

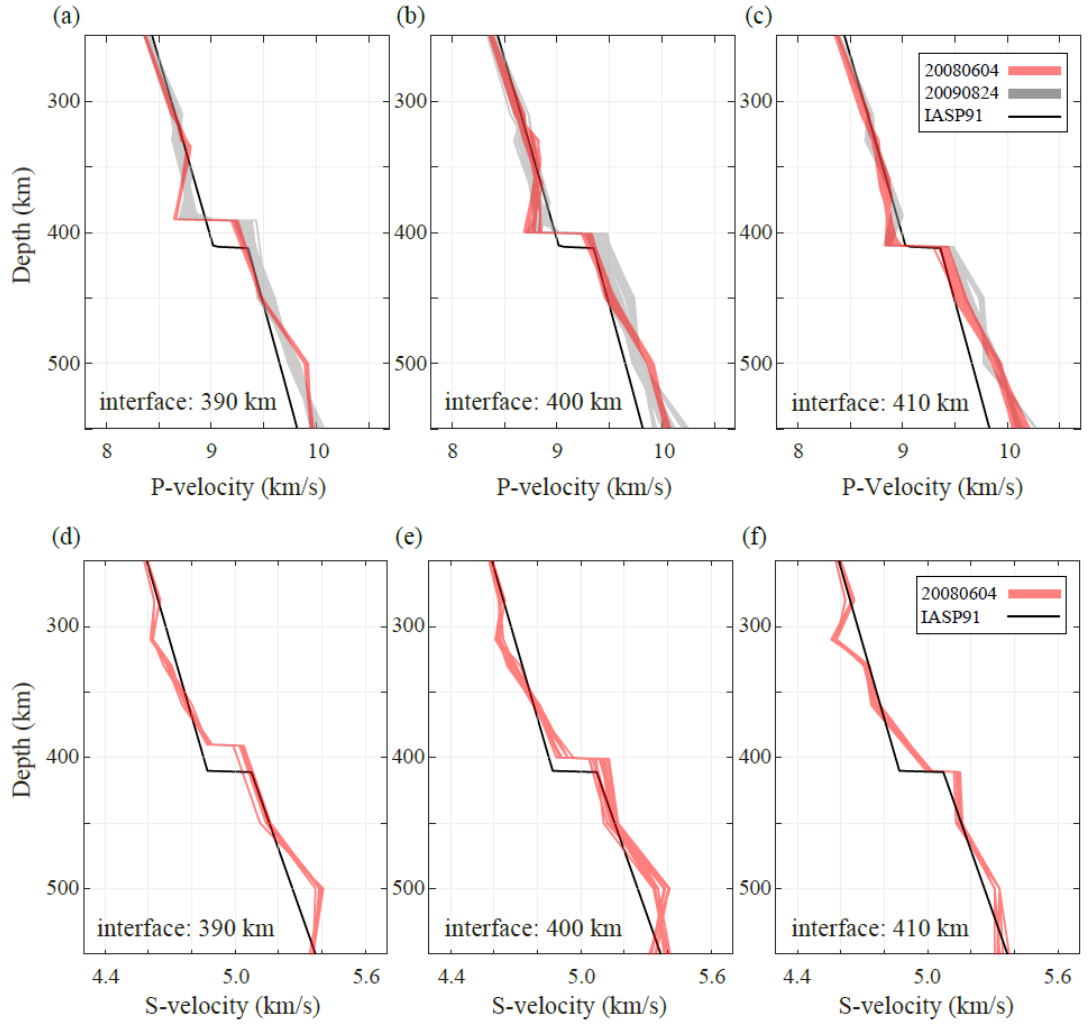
Although there are some mismatches at smaller epicentral distances between the synthetics and the data for the S waves, we interpreted it as caused by the possible noise in the data. This is because of the second peak in the waveform for stations LN.GAX or LN.BZH is of a higher frequency (i.e., shorter duration), which is inconsistent with other stations. In addition, this second peak suddenly disappears for stations at slightly smaller distances. We also performed another inversion without stations LN.GAX and LN.BZH. Results show (Fig. S1) that the waveform fitting at a smaller distance is better, and the inverted models are almost unchanged.



3.2 P-wave speed models

For the P-wave data, we performed inversions at each possible discontinuity depth from 380 km to 440 km with an interval of 10 km. There are in total 14 inversions for two events. For each event, we first found the best-fitting model with the minimum misfit (L2 norm of waveform differences) and then defined the acceptable models (e.g., shaded regions in Fig. 3) with misfits no larger than twice the minimum misfit of the best-fitting model.

For both events, there are no acceptable models when the discontinuity depths are either shallower than 390 km or deeper than 410 km. At an interface depth between 390 km and 410 km, the first-order pattern of the preferred model sets for event 20080604 (i.e., the shaded red regions in Fig. 3a and b) is similar to that for event 20090824 (i.e., the shaded blue regions in Fig. 3a and b), i.e., a low-velocity anomaly located above the discontinuity whereas the velocity at shallow depths (i.e., at around 310 km) is similar to the IASP91 model. Though with a few differences which might come from the slightly different earthquake locations, the overall consistency confirms the derived P-wave models reflect the underground structures in this region.



For most of the inverted models, there are low-velocity zones above the 410-km discontinuities compared with the IASP91 model (Kennett & Engdahl, 1991). Importantly, the size of the low-velocity zone decreases as the depth of the discontinuity increases, which exhibits the tradeoffs between these two parameters. For example, when there is no uplift (Fig. 3c), no significant low-velocity anomaly is observed in the inverted models (i.e., data can be fitted without introducing the low-velocity anomaly atop the 410-km discontinuity). However, there is a maximum P-wave reduction of 0.3 km/s when the 410-km discontinuity is uplifted by 20 km (Fig. 3a). Therefore, it is crucial to consider this tradeoff between discontinuity depth and the velocity above the discontinuity.

3.3 S-wave models

For the SH-wave inversions, the acceptable discontinuity depths are also from 390 km to 410 km (Fig. 3d-f), which are overlapped with the ranges (i.e., from 390 km to 410 km) for the P-wave inversions. Therefore, we chose these consistent depth values of 390 km and 410 km to be the preferred discontinuity depths. We further excluded the discontinuity depth of 410 km since an uplifted 410-km discontinuity should be expected in the vicinity of cold subducted slabs due to the positive Clapeyron slope of the olivine phase transition (Bina & Helffrich, 1994).

In the S-wave models (Fig. 3d-e), there is no sign of a localized low-velocity anomaly atop the 410-km discontinuity. In addition, there is another different feature from the P-wave model, i.e., a prominent low-velocity anomaly between 300 km and 360 km in the S-wave models. The existence of this shallow anomaly does not correlate with the discontinuity depth. In addition, the location of this low-velocity anomaly correlates well with the -1.5% contour in the FWEA18 model (Fig. 1c).

4. Discussions

4.1 Quasi-2D inversion

In the inverted models, one key difference between the P- and S-wave models is the location of low-velocity anomalies. The observed low-velocity anomaly in the P-wave models is localized about 30 km above the “410-km” interface. In contrast, there are two distinct low-velocity anomalies in the S-wave models, and the most considerable anomaly in the S-wave models is centered about 60 km above the “410-km” discontinuity.

However, since 1D approximation is assumed, it is essential to figure out that the different features from P and S results are not artifacts of the 1D assumption. Due to the complex 3D and 2D (i.e., in certain cross sections) structure of the subducting slab (e.g., Takeuchi et al., 2014; Tao et al., 2018), the 1D assumption might not be a reasonable approximation. For example, Wang et al. (2014), through forward modeling, proved that 2D and 3D structures affect triplication traveltime and waveforms. This influence is enhanced when the ray paths are parallel to the strike direction of the slab (Wang et al., 2014). Although, in this study, the ray paths are perpendicular to the Wadati–Benioff zone where the 2D and 3D influence is less severe (e.g., Wang et al., 2014; Han et al., 2021), we propose a new quasi-2D inversion scheme to better consider the effects of lateral variations.

In this quasi-2D inversion, we viewed the structures near the turning points (i.e., inside the dashed box in Fig. 1b) still as 1D. However, outside of this inversion box where triplications have fewer constraints, we chose the tomographic model FWEA18 as the background model. During the inversion, we kept the

values outside the box unchanged, and only modify the velocity profile inside the inversion box.

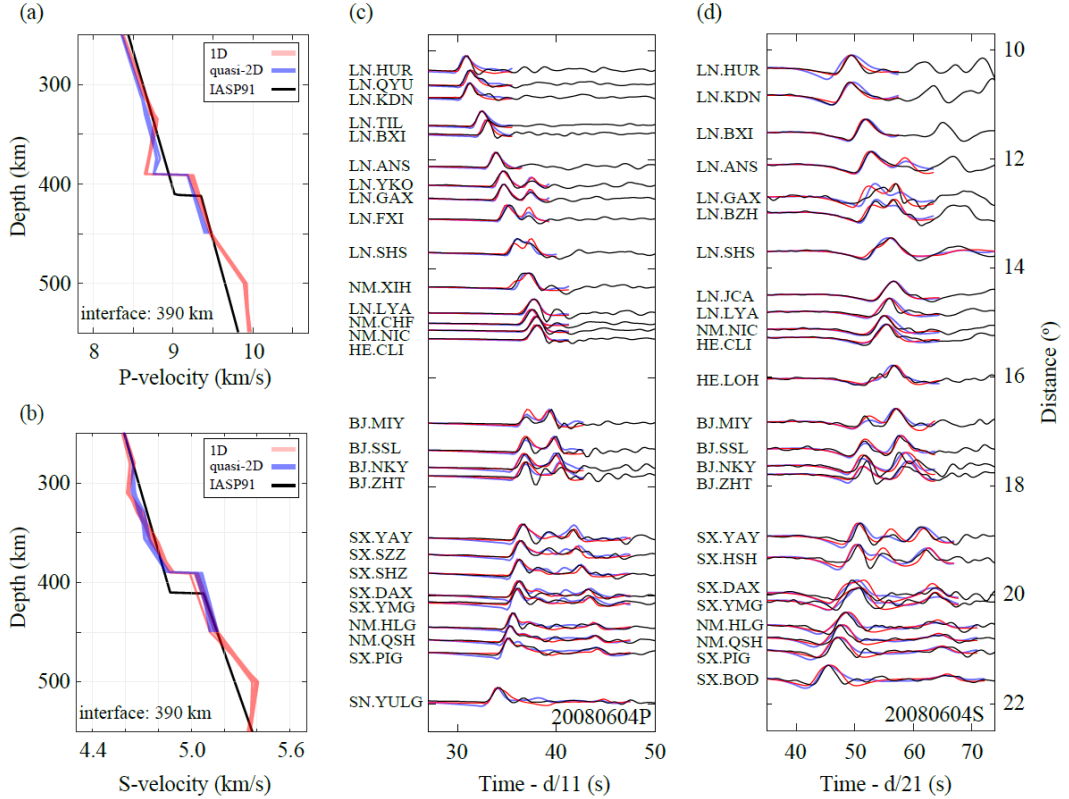
On the one hand, this quasi-2D inversion included the 2D structures near the source (i.e., the subducting slab) and receiver. On the other hand, unlike a traditional 2D inversion, this quasi-2D inversion has as few free parameters (i.e., 13 free parameters) since there is a 1D structure inside the inversion box.

Accordingly, for the forward modeling part, we have to replace the 1D software QSEIS (Wang 1999) with a GPU-based 2D finite-difference method (Li et al., 2014). We prefer a GPU-based code because, with a sufficient number of GPUs (i.e., 20 NVIDIA V100 cards), the inversion (with 10,000 forward modelings) can still be finished within one day.

For the P waves, Fig. 4a shows the waveforms fitting for the 1D inversion (in red) and quasi-2D inversion (in blue). Both synthetics match the recorded data well, and the quasi-2D inversion can improve some mismatches (e.g., LN.SHS in Fig. 4c). Fig. 4a demonstrates the difference between the inverted P-wave models (with a discontinuity depth of 390 km) for the 1D (in red) and quasi-2D (in blue) settings. The first-order pattern (i.e., the low-velocity anomaly is close to the discontinuity, and there is no other anomaly near 310 km) is the same.

For the S waves, Fig. 4d shows that the waveform fitting for the 1D (in red) and quasi-2D (in blue) settings are similar and both are acceptable. However, Fig. 4b indicates that there are some discrepancies for the inverted models from those two settings, i.e., the 1D assumption will overestimate the velocity reduction near 320 km. With the 2D correction, the shallow anomaly is still a prominent feature. Both the 1D and quasi-2D inversion results show no significant low-velocity anomaly near the discontinuity, which is different from the P-wave models.

In addition, such discrepancies between the P- and S-wave models have also been observed in the regional tomography model FWEA18 (Tao et al., 2018). Although the 3D FWEA18 model is of relatively lower resolution compared with the 1D or quasi-2D models in this study, it is a 3D inversion and thus suggests that the features we evidence are not artifacts of the 1D or quasi-2D approximation.



4.2 The shallow low-velocity zone

The mechanism of the low-velocity zone can be deciphered by the comparison between P- and S-wave models. At depths between 300 km and 370 km, there are very few low-velocity anomalies in the P-wave models from both this study (i.e., an average value of -0.4%) and the FWEA18 model (i.e., about -1.0%). However, the reduction of the S-wave velocity is at least -2.1% (e.g., Fig. 3d-e) in this study, and -1.5% in the FWEA18 model, respectively.

A high-temperature anomaly would decrease both the P- and S-wave speeds (e.g., -0.4 to -0.6 m/s/K and -0.3 to -0.4 m/s/K for the P- and S-wave speed reductions, respectively) as reported in several studies (Kern, 1982; Sinogeikin et al., 1998; Jackson et al., 2000). Consequently, this low-velocity anomaly affecting only the S waves between 300 and 370 km is not likely caused by a thermal anomaly alone.

Hydrous phases, e.g., the water-saturated olivine with 0.4% water by weight, can only lower the S-wave speeds by a very small amount (e.g, less than 1% in Mao and Li, 2016). Therefore, the prominent low-velocity anomaly in the S-wave models cannot be explained by hydrous phases alone.

However, partial melting can more significantly lower the S-wave speeds. Melt-induced reduction in the S-wave speed is always greater than that in the P-wave speed (Faul et al., 1994; Toomey et al., 1998). For example, with about 5% of melt, the reduction in the S-wave speed is twice the P-wave speed. Considering melt as a diffuse and thin grain-boundary film, it would reduce the S-wave speed by reducing the resistance to shear of grain boundaries, without significantly affecting the P-wave speed.

Moreover, a recent electrical conductivity imaging (Li et al. 2020) in the same cross-section exhibits a low-resistivity (i.e., high-conductivity) column from the root of the Changbaishan volcano down to the 410-km discontinuity (Fig. 1d). Both the location and shape of this low-resistivity region are similar to the low-velocity anomalies in the S-wave seismic model (Fig. 1c).

This is strong evidence of partial melting because resistivity is very sensitive to interconnected conductive materials. However, the source of such partial melting can originate from either slab dehydration (Huang & Zhao, 2007), or the buoyant materials coming from the lower mantle via the gap of the slab (Tang et al., 2014).

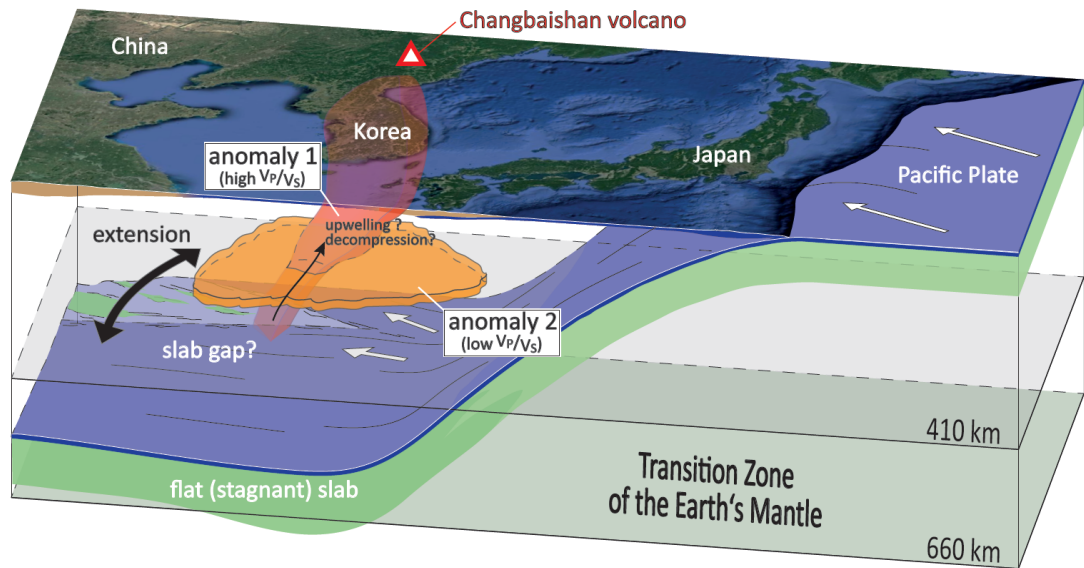
Although partial melting is favored by the observation, it is challenging to further convert the velocity reduction to the amount of partial melt, because there is large uncertainty in the relationship between the rock properties and seismic velocities (Wei & Shearer, 2017). For example, for the same S-wave speed reduction of 10%, Hier-Majumder & Tauzin (2017) and Yamauchi & Takei (2016) derived different melt estimations of 4% and 1%, respectively.

4.3 The low-velocity zone atop the 410-km discontinuity

Both the P- and S-models in the FWEA18 model exhibit low-velocity anomalies atop the 410-km discontinuity (i.e., from 120 °E to 132 °E in Fig. 1b and c). We note that the exact value of velocity reduction in the inverted results can be affected by the choice of the reference model and model parameterizations. Nevertheless, since the model parameterizations (e.g., the location of the anchor points) are the same for both the P- and S-wave models, it is reasonable to compare the first-order patterns between them. P-wave models clearly illustrate a low-velocity anomaly atop the discontinuity regardless of the interface depths and inversion approaches (i.e., 1D or quasi-2D), whereas no clear evidence for a low-velocity anomaly in the S-wave models.

Since the amplitude in the S-wave anomaly is of similar order or even smaller than that of the P-waves in both the FWEA18 model (Fig. 1b and c) and our velocity-depth profiles (Fig. 3), this anomaly cannot be caused by partial melting alone. Such an anomaly atop the 410-km discontinuity should not be caused by high temperature because the inverted 410-km depth is no deeper than 410 km (Fig. 3). The positive Clapeyron slope of the olivine-wadsleyite phase transition indicates that the temperature atop the 410-km should be cooler than the ambient mantle.

Our result can be viewed as an ‘anchor point’ (i.e., an average 1-D model in the dashed box in Fig. 1b and c) of the FWEA18 model since our method is most sensitive to the turning points of the ray paths (i.e., shown in Fig. 1d, in black). In addition, we considered different discontinuity depths and all possible interface locations exhibit consistent conclusions. Thus, our results confirm that the features in the FWEA18 model in the vicinity of the 410-km discontinuity are not artifacts either due to the damping or the fixed discontinuity depth during the full-waveform inversion. We note that the FWEA18 model shows that this low-velocity anomaly extends to a wider horizontal scale (i.e., from 120 °E to 132 °E). Therefore, we propose that this localized low-velocity anomaly is likely caused by the reduction of the effective moduli during the phase transformation (Anderson 1998; Jackson, 2007). In zones where olivine (low-pressure phase) and wadsleyite (high-pressure phase) coexist (e.g., a thickness of 10 km for the 410-km discontinuity (Durand et al., 2012)), any pressure perturbation by a passing seismic wave (e.g., on the order of $\sim 10^{-7}$ GPa) would disrupt the equilibrium and potentially induce the phase transformation in one way or the other (Li et al., 2008). Durand et al. (2012) showed that this transformation loop does not affect S waves, but potentially influences the P waves. This is consistent with the more prominent P-wave speed reduction in both the FWEA18 model and our study. In addition, since this mechanism is related to the phase transition, it would explain why the low-velocity anomaly is only limited to the region atop the 410-km discontinuity.



5. Conclusions

The upper mantle beneath the Changbaishan volcano is characterized by two seismic low-velocity anomalies with distinct seismic velocity (i.e., P- and S-wave) features and cannot be explained by the same mechanism.

We selected two earthquakes and a sub-linear array to perform high-resolution 1D and quasi-2D inversions. Our derived velocity-depth profile can be viewed as a high-resolution ‘anchor point’ in the cross-section of the full-waveform inversion model FWEA18 and confirms the distinct behaviors of the P- and S-wave models in the FWEA18 model (Fig. 1b and c). Complementary electrical conductivity imaging also exhibits a column of low-resistance anomaly from the 410-km discontinuity up the root of the Changbaishan volcano.

Based on the above evidence, we propose that the two distinct low-velocity anomalies in the upper mantle cannot be explained by the same mechanism. Near the 410-km discontinuity, the low-velocity anomaly would be caused by the reduction of the effective moduli during the phase transformation (e.g., Durand et al. 2012). However, the other low-velocity anomaly which mostly affects the S-waves and the associated high electrical conductivity between 200 and 370 km is more likely caused by partial melting which can originate either slab dehydration (Huang & Zhao, 2007), or the buoyant materials coming from the possible gap of the slab (Tang et al., 2014).

Open Research

The software FastTrip used to perform the waveform inversion is freely accessible (<https://github.com/lijiaqi0315/FastTrip>, doi:10.5281/zenodo.6392194). Waveform data for this study are provided by Data Management Centre of China National Seismic Network at Institute of Geophysics (SEISDMC, doi:10.11998/SeisDmc/SN, <http://www.seisdmc.ac.cn>). Datasets for this research are included in Zheng et al., (2020), DOI: 10.1785/0120090257.

Acknowledgment

We thank Xianbing Zhang (Peking University) for technical help and Daoyuan Sun (University of Science and Technology of China) for the discussions. Shaohua Li is supported by Major science and technology projects of Gansu Province (21ZD4FA011), Earthquake Science and Technology Development Fund, Gansu Earthquake Agency (2021Y10), and Science for Earthquake Resilience, China Earthquake Administration (XH19043). The work was carried out at National Supercomputer Center in Tianjin, and the calculations were performed on TianHe-1A.

References

1. Anderson, D.L. 1998. The scales of mantle convection. *Tectonophysics* 284(1-2),1-17.
2. Bina, C. R., & Helffrich, G. (1994). Phase transition Clapeyron slopes and transition zone seismic discontinuity topography. *Journal of Geophysical Research: Solid Earth*, 99(B8), 15853-15860.
3. Bissig, F., Khan, A., & Giardini, D. (2022). Evidence for basalt enrichment in the mantle transition zone from inversion of triplicated P-and S-waveforms. *Earth and Planetary Science Letters*, 580, 117387.
4. Bozdag, E., Peter, D., Lefebvre, M., Komatitsch, D., Tromp, J., Hill, J., ... & Pugmire, D. (2016). Global adjoint tomography: first-generation model. *Geophysical Journal International*, 207(3), 1739-1766.
5. Chen, M., Niu, F., Liu, Q., Tromp, J., & Zheng, X. (2015). Multiparameter adjoint tomography of the crust and upper mantle beneath East Asia: 1. Model construction and comparisons. *Journal of Geophysical Research: Solid Earth*, 120(3), 1762-1786.
6. Chen, Y., Zhang, Y., Graham, D., Su, S., & Deng, J. (2007). Geochemistry of Cenozoic basalts and mantle xenoliths in Northeast China. *Lithos*, 96(1-2), 108-126.
7. Chen, Y. J., & Pei, S. (2010). Tomographic structure of East Asia: II. Stagnant slab above 660 km discontinuity and its geodynamic implications. *Earthquake Science*, 23(6), 613-626.
8. Durand, S., Chambat, F., Matas, J. & Ricard, Y., 2012. Constraining the kinetics of mantle phase changes with seismic data. *Geophysical Journal International* 189(3),1557-1564.
9. Ekstrom, G., Nettles, M., & Dziewoński, A. M. (2012). The global CMT project 2004–2010: Centroid-moment tensors for 13,017 earthquakes. *Physics of the Earth and Planetary Interiors*, 200, 1-9.
10. Faul, U. H., Toomey, D. R., & Waff, H. S. (1994). Intergranular basaltic melt is distributed in thin, elongated inclusions. *Geophysical Research Letters*, 21(1), 29-32.
11. Fichtner, A., Kennett, B. L., Igel, H., & Bunge, H. P. (2009). Full seismic waveform tomography for upper-mantle structure in the Australasian region using adjoint methods. *Geophysical Journal International*, 179(3), 1703-1725.
12. French, S. W., & Romanowicz, B. A. (2014). Whole-mantle radially anisotropic shear velocity structure from spectral-element waveform tomography. *Geophysical Journal International*, 199(3), 1303-1327.

13. Han, G., Li, J., Guo, G., Mooney, W. D., Karato, S. I., & Yuen, D. A. (2021). Pervasive low-velocity zone atop the 410-km discontinuity beneath the northwest Pacific subduction zone: Implications for rheology and geodynamics. *Earth and Planetary Science Letters*, 554, 116642.
14. Hayes, G.P., Moore, G.L., Portner, D.E., Hearne, M., Flamme, H., Furtney, M. and Smoczyk, G.M., 2018. Slab2, a comprehensive subduction zone geometry model. *Science*, 362(6410), pp.58-61.
15. Hier-Majumder, S., & Tauzin, B. (2017). Pervasive upper mantle melting beneath the western US. *Earth and Planetary Science Letters*, 463, 25-35.
16. Huang, J., & Zhao, D. (2006). High-resolution mantle tomography of China and surrounding regions. *Journal of Geophysical Research: Solid Earth*, 111(B9).
17. Jackson, I. 2007. In *Treatise on Geophysics Vol. 2* (ed. Schubert, G.) 493–525.
18. Jackson, J. M., Sinogeikin, S. V., & Bass, J. D. (2000). Sound velocities and elastic properties of $\text{-Mg}_2\text{SiO}_4$ to 873 K by Brillouin spectroscopy. *American Mineralogist*, 85(2), 296-303.
19. Kennett, B.L.N. & Engdahl, E.R. 1991. Traveltimes for global earthquake location and phase identification. *Geophysical Journal International* 105(2), 429-465.
20. Kern, H. (1982). P-and S-wave velocities in crustal and mantle rocks under the simultaneous action of high confining pressure and high temperature and the effect of the rock microstructure.
21. Komatitsch, D., & Tromp, J. (1999). Introduction to the spectral element method for three-dimensional seismic wave propagation. *Geophysical journal international*, 139(3), 806-822.
22. Koper, K.D., Wyssession, M.E. & Wiens, D.A. 1999. Multimodal function optimization with a niching genetic algorithm: A seismological example. *Bulletin of the Seismological Society of America* 89(4),978-988.
23. Kuritani, T., Ohtani, E., & Kimura, J. I. (2011). Intensive hydration of the mantle transition zone beneath China caused by ancient slab stagnation. *Nature Geoscience*, 4(10), 713-716.
24. Lei, W., Ruan, Y., Bozdag, E., Peter, D., Lefebvre, M., Komatitsch, D., ... & Pugmire, D. (2020). Global adjoint tomography—model GLAD-M25. *Geophysical Journal International*, 223(1), 1-21.
25. Li, D., Helmberger, D., Clayton, R.W. and Sun, D., 2014. Global synthetic seismograms using a 2-D finite-difference method. *Geophysical Journal International*, 197(2), pp.1166-1183.

26. Li, J., Chen, M., Koper, K. D., Zhou, T., Xi, Z., Li, S., & Li, G. (2021). FastTrip: A Fast MPI-Accelerated 1D Triplication Waveform Inversion Package for Constraining Mantle Transition Zone Discontinuities. *Seismological Society of America*, 92(4), 2647-2656.
27. Li, J., Chen, M., Ning, J., Bao, T., Maguire, R., Flanagan, M. P., & Zhou, T. (2022). Constraining the 410-km discontinuity and slab structure in the Kuril subduction zone with triplication waveforms. *Geophysical Journal International*, 228(2), 729-743.
28. Li, L. & Weidner, D.J. 2008. Effect of phase transitions on compressional-wave velocities in the Earth's mantle. *Nature* 454(7207), 984-986.
29. Li, S., Weng, A., Li, J., Shan, X., Han, J., Tang, Y., ... & Wang, X. (2020). Deep origin of Cenozoic volcanoes in Northeast China revealed by 3-D electrical structure. *Science China Earth Sciences*, 63(4), 533-547.
30. Mao, Z., & Li, X. (2016). Effect of hydration on the elasticity of mantle minerals and its geophysical implications. *Science China Earth Sciences*, 59(5), 873-888.
31. Sinogeikin, S. V., Katsura, T., & Bass, J. D. (1998). Sound velocities and elastic properties of Fe-bearing wadsleyite and ringwoodite. *Journal of Geophysical Research: Solid Earth*, 103(B9), 20819-20825.
32. Shearer, P.M., 2000. Upper mantle seismic discontinuities. *GEOPHYSICAL MONOGRAPH-AMERICAN GEOPHYSICAL UNION*, 117, pp.115-132.
33. Stahler, S. C., Sigloch, K., & Nissen-Meyer, T. (2012). Triplicated P-wave measurements for waveform tomography of the mantle transition zone. *Solid Earth*, 3(2), 339-354.
34. Stein S., Wysession M., 2009. *An Introduction to Seismology, Earthquakes, and Earth Structure*. John Wiley & Sons.
35. Takeuchi, N., Kawakatsu, H., Tanaka, S., Obayashi, M., Chen, Y.J., Ning, J., Grand, S.P., Niu, F., Ni, J., Iritani, R. and Idehara, K., 2014. Upper mantle tomography in the northwestern Pacific region using triplicated P waves. *Journal of Geophysical Research: Solid Earth*, 119(10), pp.7667-7685.
36. Tang, Y., Obayashi, M., Niu, F., Grand, S. P., Chen, Y. J., Kawakatsu, H., ... & Ni, J. F. (2014). Changbaishan volcanism in northeast China linked to subduction-induced mantle upwelling. *Nature Geoscience*, 7(6), 470-475.
37. Tao, K., Grand, S.P. & Niu, F., 2018. Seismic structure of the upper mantle beneath eastern Asia from full waveform seismic tomography. *Geochemistry, Geophysics, Geosystems* 19(8),2732-2763.

38. Tape, C., Liu, Q., Maggi, A., & Tromp, J. (2009). Adjoint tomography of the southern California crust. *Science*, 325(5943), 988-992.
39. Tatsumi, Y., Maruyama, S., & Nohda, S. (1990). Mechanism of backarc opening in the Japan Sea: role of asthenospheric injection. *Tectonophysics*, 181(1-4), 299-306.
40. Toomey, D. R., Wilcock, W. S., Solomon, S. C., Hammond, W. C., & Orcutt, J. A. (1998). Mantle seismic structure beneath the MELT region of the East Pacific Rise from P and S wave tomography. *Science*, 280(5367), 1224-1227.
41. Tromp, J., Tape, C., & Liu, Q. (2005). Seismic tomography, adjoint methods, time reversal and banana-doughnut kernels. *Geophysical Journal International*, 160(1), 195-216.
42. Tseng, T. L., & Chen, W. P. (2008). Discordant contrasts of P-and S-wave speeds across the 660-km discontinuity beneath Tibet: A case for hydrous remnant of sub-continental lithosphere. *Earth and Planetary Science Letters*, 268(3-4), 450-462.
43. Wang, R. 1999. A simple orthonormalization method for stable and efficient computation of Green's functions. *Bulletin of the Seismological Society of America* 89(3), 733-741.
44. Wang, T., Revenaugh, J., & Song, X. (2014). Two-dimensional/three-dimensional waveform modeling of subducting slab and transition zone beneath Northeast Asia. *Journal of Geophysical Research: Solid Earth*, 119(6), 4766-4786.
45. Wei, S.S. & Shearer, P.M. 2017. A sporadic low-velocity layer atop the 410 km discontinuity beneath the Pacific Ocean. *JGR Solid Earth*, 122(7), 5144-5159.
46. Yamauchi, H., & Takei, Y. (2016). Polycrystal anelasticity at near-solidus temperatures. *Journal of Geophysical Research: Solid Earth*, 121(11), 7790-7820.
47. Zhao, D., Tian, Y., Lei, J., Liu, L., & Zheng, S. (2009). Seismic image and origin of the Changbai intraplate volcano in East Asia: Role of big mantle wedge above the stagnant Pacific slab. *Physics of the Earth and Planetary Interiors*, 173(3-4), 197-206.
48. Zheng, X.F., Yao, Z.X., Liang, J.H. & Zheng, J. 2010. The role played and opportunities provided by IGP DMC of China National Seismic Network in Wenchuan earthquake disaster relief and researches. *Bulletin of the Seismological Society of America* 100(5B), 2866-2872.
49. Zhu, H., Bozdag, E., & Tromp, J. (2015). Seismic structure of the European upper mantle based on adjoint tomography. *Geophysical Journal International*, 201(1), 18-52.

50. Zou, H., Fan, Q., & Yao, Y. (2008). U–Th systematics of dispersed young volcanoes in NE China: asthenosphere upwelling caused by piling up and upward thickening of stagnant Pacific slab. *Chemical Geology*, 255(1-2), 134-142.